



Frictional properties and microstructural evolution of dry and wet calcite-dolomite gouges

Matteo Demurtas¹, Steven A.F. Smith², Elena Spagnuolo³, and Giulio Di Toro^{3,4}

¹Physics of Geological Processes, The Njord Centre, Department of Geosciences, University of Oslo, Oslo, Norway

²Department of Geology, University of Otago, Dunedin 9054, New Zealand

³Istituto Nazionale di Geofisica e Vulcanologia (INGV), Rome 00143, Italy

⁴Dipartimento di Geoscienze, Università degli Studi di Padova, 35131 Padova, Italy

Correspondence: Matteo Demurtas (matteodemu@gmail.com)

Abstract. Calcite and dolomite are the two most common minerals in carbonate-bearing faults and shear zones. Motivated by field examples from exhumed seismogenic faults in the Italian Central Apennines, we investigated the frictional and microstructural evolution of gouge mixtures consisting of 50 wt.% calcite and 50 wt.% dolomite using a rotary-shear apparatus. The gouges were sheared at a range of slip rates ($30 \mu\text{ms}^{-1}$ – 1ms^{-1}), displacements (0.05–0.4 m), and normal loads (17.5–26 MPa), under both room humidity and water-dampened conditions. The frictional behaviour and microstructural evolution of the gouges were strongly influenced by the presence of water. At room humidity, slip strengthening behaviour was observed up to slip rates of 0.01ms^{-1} , which was associated with gouge dilation and the development of a 500–900 μm wide slip zone cut by Y-, R-, and R_1 -shear bands. Above a slip rate of 0.1ms^{-1} , dynamic weakening accompanied the development of a localised $<100 \mu\text{m}$ thick principal slip zone preserving microstructural evidence for calcite recrystallization and dolomite decarbonation, while the bulk gouges developed a well-defined foliation consisting of organized domains of heavily fractured calcite and dolomite. In water-dampened conditions, evidence of gouge fluidization within a fine-grained principal slip zone was observed at a wide range of slip-rates from $30 \mu\text{ms}^{-1}$ to 0.1ms^{-1} , suggesting that caution is needed when relating fluidization textures to seismic slip in natural fault zones. Dynamic weakening in water-dampened conditions was observed at 1ms^{-1} , where the principal slip zone was characterised by patches of recrystallized calcite. However, local fragmentation and reworking of recrystallized calcite suggests a cyclic process involving formation and destruction of a heterogeneous slip zone. Our microstructural data show that development of a well-defined gouge foliation at these experimental conditions is limited to high-velocity ($>0.1 \text{ms}^{-1}$) and room humidity, supporting the notion that some foliated gouges and cataclasites may form during seismic slip in natural carbonate-bearing faults.

1 Introduction

Calcite and dolomite are the most common minerals in carbonate-bearing faults and shear zones (e.g. Busch and van der Pluijm, 1995; Snoke et al., 1998; Bestmann et al., 2000; De Paola et al., 2006; Molli et al., 2010; Tesei et al., 2014; Fondriest et al., 2015, 2020; Delle Piane et al., 2017). In many cases, the distribution and timing of dolomitization plays an important role in controlling where strain localization occurs. For example, ductile deformation along the Naukluft Nappe Complex in



central Namibia was distributed within a sequence of calcite mylonites, but the main Naukluft Fault formed within heavily
25 dolomitized layers (Viola et al., 2006; Miller et al., 2008).

Although similar in composition, the rheology, deformation mechanisms, and frictional behaviour of calcite and dolomite
show important differences. Calcite has been widely investigated using microstructural analysis (Kennedy and Logan, 1997;
Kennedy and White, 2001; Liu et al., 2002; Bestmann et al., 2006; Molli et al., 2011) and laboratory experiments over a wide
range of deformation conditions, which includes experiments performed at relatively low strain rates, high temperatures, and
30 high pressures (e.g. Rutter, 1972; Schmid et al., 1980, 1987; De Bresser and Spiers, 1990; Rutter, 1995; Paterson and Olgaard,
2000), and experiments performed at relatively high strain rates, low temperatures, and low pressures (Smith et al., 2013,
2015; Verberne et al., 2014; De Paola et al., 2015; Rempe et al., 2017; Tesei et al., 2017). Comparatively, the rheology and
frictional behaviour of dolomite are relatively poorly understood (e.g. Barber et al., 1981; Weeks and Tullis, 1985). Recently,
the importance of dolomite as a fault and shear zone material in sedimentary and metamorphic settings has been emphasized
35 in a number of experimental studies (Austin and Kennedy, 2005; Delle Piane et al., 2007, 2008; Davis et al., 2008; De Paola
et al., 2011a, b; Fondriest et al., 2013; Holyoke et al., 2014). At low strain rates, dolomite is brittle up to c. 700 °C (Kushnir
et al., 2015), while calcite can deform plastically at temperatures as low as 150–200 °C (Kennedy and White, 2001). This
pronounced difference in deformation style under similar ambient conditions may significantly influence the rheology of faults
and shear zones in which the two phases co-exist. For example, the occurrence of patches or dispersed grains of dolomite
40 within calcite-mylonites can result in more efficient strain localization (Oesterling et al., 2007; Kushnir et al., 2015).

Only a few experimental studies have investigated the mechanical behaviour and microstructural evolution of calcite-
dolomite mixtures. Experiments have been performed to study the rheological behaviour of mixtures at relatively high pressures
and temperatures (e.g. torsion experiments of Delle Piane et al., 2009; Kushnir et al., 2015), as well as the frictional behaviour
of mixtures at room temperature over a wide range of strain rates (e.g. room temperature rotary-shear experiments: Mitchell et
45 al., 2015; Smith et al., 2017; Demurtas et al., 2019a, b). In torsion experiments (confining pressures up to 300 MPa, tempera-
tures of 700–800 °C, shear strain rate $\dot{\gamma} = 1-3 \times 10^{-4} \text{ s}^{-1}$, and finite shear strain $\gamma < 11$), minor quantities of dolomite (e.g. 25
wt.%) in a sintered calcite-rich sample significantly increased the yield strength with respect to pure calcite samples (Kushnir
et al., 2015). Under such experimental conditions, two main deformation mechanisms were observed: brittle fracturing in the
dolomite grains and ductile flow in calcite, possibly as a result of grain boundary sliding assisted by diffusion creep and dislo-
cation glide (Kushnir et al., 2015). Strain hardening observed in these experiments was interpreted to be due to dolomite grains
50 interrupting more continuous calcite-rich layers and acting as stress concentrators. Brittle failure of dolomite grains eventually
allowed the calcite-rich layers to become continuous and to continue deforming by superplastic flow (Kushnir et al., 2015).

Mitchell et al. (2015) and Smith et al. (2017) studied the frictional behaviour and microstructural evolution of gouge mix-
tures (50 wt.% dolomite and 50 wt.% calcite) deformed at low normal stresses ($\sigma_n \leq 17.5 \text{ MPa}$), high slip rates ($V \geq 0.01$
55 ms^{-1}), and large displacements ($d = 0.03-3 \text{ m}$), with the aim of reproducing conditions encountered at the base of fast-moving
landslides and during the seismic cycle in shallow-crustal faults. At a slip velocity of 1 ms^{-1} , dynamic weakening was associ-
ated with grain size reduction and decarbonation of dolomite within the experimental principal slip zone and in the nearby bulk
gouge. During the early stages of these high-velocity experiments, and prior to the onset of dynamic weakening, a well-defined



foliation developed within the gouge mixtures due to brittle fracturing of calcite and dolomite accompanied by shearing of the fractured grains in to compositional bands (Mitchell et al., 2015; Smith et al., 2017). These observations indicate that some natural examples of foliated gouges and cataclasites could form during coseismic shearing (Smith et al., 2017), challenging the common interpretation that fault rock foliations result from slow aseismic creep (e.g. Rutter et al., 1986; Chester and Chester, 1998; Lin, 2001; Jefferies et al., 2006). Additionally, Demurtas et al. (2019a) documented the presence of a well-defined crystallographic preferred orientation (CPO) in calcite-dolomite gouges, and interpreted the CPO to result from “brittle” processes involving grain rotation and preferential fracturing along calcite cleavage planes during granular flow at room temperature. Instead, in regions of the mixed gouge layers that experienced substantial frictional heating during high-velocity slip (i.e. within the principal slip zone), Transmission Kikuchi Diffraction analysis suggested that nanogranular aggregates deformed by a combination of grain size sensitive (grains <800 nm) and grain size insensitive (grains >800 nm) plastic creep (Demurtas et al., 2019b).

The experimental work summarized above indicates that a diverse range of microstructures can form in calcite-dolomite gouges as a result of both brittle and plastic processes, and that the prevailing microstructures depend on ambient conditions, strain history, and proximity to zones of shear localization and heating. Potentially, this range of microstructures could be recognized in natural gouges and cataclasites, which would provide important insights in to the evolution of slip conditions during the seismic cycle in carbonate-bearing faults. However, to successfully apply the experimental findings to natural fault zones, a more complete picture of microstructural diversity and its dependence on deformation conditions is required. In this context, the aim of this paper is to provide (i) a more comprehensive description of the frictional and microstructural evolution of mixed calcite-dolomite gouges deformed at sub-seismic to seismic slip rates, and (ii) an updated framework for the interpretation of microstructures found in natural calcite- and dolomite-bearing faults.

2 Methods

2.1 Starting materials

Synthetic gouges were prepared by mixing 50 wt.% calcite and 50 wt.% dolomite as previously described in Demurtas et al. (2019a). The calcite-dolomite ratio in the experimental mixtures is similar to that found in natural fault gouges and cataclasites from the Vado di Corno Fault Zone (VCFZ, Italian Central Apennines; Demurtas et al., 2016), and used in previous experimental studies (Smith et al., 2017). The calcite gouge was derived by crushing Carrara marble with a modal composition of 98.8 wt.% calcite and <1 wt.% dolomite and muscovite (see Supplementary Material). The dolomite gouge was derived by crushing dolomitized portions of the Calcare Massiccio Formation from the VCFZ (Demurtas et al., 2016). The crushed gouges were passed through a 250 μm sieve and then mixed together by slow tumbling for c. 30 minutes. Two batches of gouge were prepared (CDM1, calcite = 47.2 wt.% and dolomite = 52.8 wt.%; CDM2, calcite = 42.9 wt.% and dolomite = 57.1 wt.%).



2.2 Experimental setup and deformation conditions

90 Nineteen experiments were performed at slip rates from $30 \mu\text{ms}^{-1}$ to 1ms^{-1} with SHIVA (Slow- to High-Velocity rotary-shear friction Apparatus) at the Istituto Nazionale di Geofisica e Vulcanologia in Rome (Di Toro et al., 2010; Niemeijer et al., 2011) (Table 1). The gouges were deformed inside a metal holder specifically designed for incohesive materials (Fig. 1; Smith et al., 2013, 2015). The thickness of the gouge layers at the start of the experiments was c. 3 mm. Horizontal displacements of the axial column were sampled at 2.5 Hz–25 kHz, and measured using a direct current differential transformer (DCDT, 50 mm
95 range and c. $50 \mu\text{m}$ resolution) and a linear variable differential transformer (LVDT, 3 mm range and c. $0.03 \mu\text{m}$ resolution). Further details of the data acquisition system, and location and calibration of the load cells, detectors, and devices, are found in Niemeijer et al. (2011) and Smith et al. (2013).

Measurements of room humidity and room temperature were collected at a distance of $<1 \text{cm}$ from the gouge holder before and during the experiments (Fig. 1a). Temperature variations during deformation were measured at an acquisition rate of 2.5
100 Hz using four K-type thermocouples (Nickel-Alumel) installed on the stationary side of the gouge holder (Fig. 1a-b; Demurtas et al., 2019a). One thermocouple was positioned at c. $200 \mu\text{m}$ from the gouge layer (Fig. 1b). The other three thermocouples were located in the sample holder and stationary column to detect temperature variations due to heat conduction through the gouge holder and apparatus (Fig. 1a). CO_2 emissions were monitored using an OmniStar™ GSD 301 O mass spectrometer designed for gas analysis at atmospheric pressure.

105 Experiments were performed at both room humidity and water-dampened conditions with normal stress held constant at $17.5 \pm 0.1 \text{MPa}$, with the exception of experiment *s1324* performed at 26 MPa normal stress (Table 1). Room humidity varied between 41% and 62%, and the room temperature between 19°C and 22°C . In water-dampened conditions, c. 2 ml of deionized water was added to the top of the gouge layer using a pipette before the gouge holder was positioned in the apparatus. Experiment *s1327* was performed using a specially designed water bath that ensured saturation within the gouge layer during this long-duration experiment (Supplementary Material). Experiments were performed at target slip rates ranging from $30 \mu\text{ms}^{-1}$ to 1ms^{-1} , with acceleration and deceleration of 6ms^{-2} . Total displacements ranged from 0.05 m to 0.4 m. Two compaction experiments were performed by applying a normal stress of 17.5 MPa for 300 s (i.e. static load experiments in Table
110 1) and used as references for the microstructure of the starting materials.

2.3 Analytical techniques

115 After each experiment, the entire gouge layer was recovered and impregnated in low-viscosity epoxy (Araldite 2020) for microstructural analysis. Polished thin sections were cut perpendicular to the gouge layer and subparallel (i.e. tangential cut) to the slip direction (Fig. 1d). Microstructural analysis was performed with a Zeiss Sigma VP Field-Emission Scanning Electron Microscope (SEM) at the Otago Micro and Nanoscale Imaging facility (OMNI; University of Otago. Acquisition conditions for backscattered electron images: accelerating voltage 15 kV, working distance 6-7 mm). Energy-dispersive X-ray spectroscopy (EDS) in the SEM was used to produce element maps showing the distribution of calcium and magnesium. Crystallographic
120 orientation data from calcite were acquired by electron backscatter diffraction (EBSD) on SYTON-polished thin sections.



Data were collected with a NordlysF EBSD camera from Oxford Instruments and processed using AZtec software (Oxford Instruments). Mineralogical changes that occurred during the experiments were determined by semi-quantitative X-ray powder diffraction (XRPD) conducted in the Department of Geoscience, University of Padova. The XRPD analyses were performed on both the bulk gouges and on small intact chips of the localized slip surfaces that formed in the experiments.

3 Results

3.1 Friction evolution with slip and slip rate

The evolution of the effective friction coefficient (μ) with slip and slip rate was influenced by the availability of water during deformation (Figs. 2, 3). In room humidity conditions and slip rates ≤ 0.01 ms⁻¹, the calcite-dolomite mixtures showed a progressive increase of μ (slip strengthening behaviour) up to 0.75-0.80 (measured between 0.15 m and 0.35 m of slip) following an initial peak friction (μ_{peak}) of 0.64-0.71 (Figs. 2, 3). At a slip rate of 0.1 ms⁻¹, a substantial decrease of μ was observed (slip weakening behaviour to steady state μ_{ss} of 0.55 ± 0.01) following a prolonged initial strengthening phase (c. 0.062 m) that reached μ_{peak} of 0.68 (Fig. 2b). Significant dynamic weakening was observed at a slip rate of 1 ms⁻¹ at 17.5 MPa and 26 MPa normal stress (experiments *s1221* and *s1324*, respectively), following a short initial strengthening phase (lasting c. 0.005-0.008 m) that was followed by a steady state of μ_{ss} of 0.25-0.28 (Figs. 2a, 3b). In these two experiments, a re-strengthening phase (final μ up to c. 0.56-0.59) was observed during deceleration of the rotary column.

In water-dampened conditions, the gouge mixtures showed a similar evolution of friction at slip rates ≤ 0.1 ms⁻¹, characterized by slight slip strengthening to slip neutral behaviour (Fig. 2c). Notably, μ_{peak} and μ_{ss} were lower than in room humidity experiments, with $\mu_{\text{peak}} = 0.61-0.64$ and $\mu_{\text{ss}} = 0.62-0.70$ (Fig. 3). At a slip rate of 1 ms⁻¹, the initial strengthening phase was much shorter than in room-humidity conditions (c. 0.003 m), and dynamic weakening resulted in μ_{ss} of 0.31 ± 0.02 . Re-strengthening was also observed during deceleration, with an increase in μ up to 0.57.

3.2 Gouge thickness evolution with slip rate

No significant gouge loss was observed during the experiments, with the exception of those performed at $V = 0.1$ ms⁻¹ discussed below. Therefore, the evolution of axial displacement is interpreted to result from changes in gouge layer thickness due to dilation and compaction. In room humidity conditions, the evolution of gouge layer thickness depends on slip rate (Fig. 4a). At $V \leq 0.001$ ms⁻¹, the gouge layers show a three-stage evolution: (i) initial compaction of c. 90-120 μm at the onset of sliding, (ii) dilation of c. 50-70 μm during the slip strengthening phase, and (iii) approximately constant thickness once the steady state friction coefficient is reached. Overall compaction of c. 30-60 μm is recorded. At $V = 0.01$ ms⁻¹, initial compaction of 100 μm is followed by approximately constant thickness (Fig. 4a). At higher slip rates ($V \geq 0.1$ ms⁻¹), continuous compaction was observed throughout the experiments (up to c. 300 μm of axial shortening at $V = 1$ ms⁻¹), and compaction rate increased with slip rate (Fig. 4a).



Under water-dampened conditions, the gouge mixtures exhibit a similar evolution of thickness irrespective of slip rate (Fig. 4b). Compaction was initially rapid in the first few cm of sliding, and then reached an approximately constant compaction rate that was similar in all experiments. Total compaction of c. 200-250 μm was recorded (Fig. 4b).

155 3.3 Temperature evolution and CO₂ emissions

Figure 5a shows maximum temperatures measured by the thermocouple located closest to the gouge layers (Fig. 1b; Demurtas et al., 2019a, described temperature evolution with slip). The maximum temperature (621 °C) was achieved in experiment *sI221* performed under room humidity conditions at $V = 1 \text{ ms}^{-1}$ (Fig. 5a). For the same slip rate and normal stress, but in water-dampened conditions, the maximum temperature was 210 °C (Fig. 5a). Temperature increases were detected in all 160 experiments at slip rates $\geq 0.01 \text{ ms}^{-1}$, and the maximum temperature increased with increasing slip rate (Fig. 5a).

CO₂ emissions above ambient levels were only detected in experiments at slip rates $\geq 0.1 \text{ ms}^{-1}$ (Fig. 5b). Because the mass spectrometer was not calibrated and the sample holder was open to the laboratory, the data can only be used in a qualitative way. In room humidity conditions, the intensity of the CO₂ peak was significantly higher at 1 ms^{-1} than at 0.1 ms^{-1} . In water-dampened conditions, the CO₂ peaks were substantially smaller than at equivalent room humidity conditions.

165 3.4 Mineralogy of deformed gouges

Compared to the starting materials, no mineralogical changes were detected in any of the deformed bulk gouges (see Supplementary Material). In room humidity experiment *sI210* ($30 \mu\text{ms}^{-1}$), a slight broadening of the main peak for calcite was observed (Fig. 6a), and to a lesser degree also for dolomite. XRPD analysis of cohesive chips recovered from the slip surface of water-dampened experiment *sI214* ($V = 30 \mu\text{ms}^{-1}$) indicates the presence of aragonite (Fig. 6b). At $V = 1 \text{ ms}^{-1}$ and room humidity 170 conditions, the recovered slip surface was composed of dolomite, Mg-calcite, and periclase (MgO) (Fig. 6c). Mg-calcite and periclase are two of the main products of dolomite decarbonation that starts at c. 550 °C ($\text{MgCa}(\text{CO}_3)_2 \rightarrow \text{MgO} + (\text{Ca}, \text{Mg})\text{CO}_3 + \text{CO}_2$, Samtani et al., 2002; De Paola et al., 2011a, b).

3.5 Microstructures of deformed gouge layers

Figure 7 summarizes the range of microstructures that developed in room humidity and water-saturated conditions at different 175 slip rates. As noted in previous experiments (e.g. Kitajima et al., 2010; Smith et al., 2017), several distinct microstructures and microstructural domains were recognized, defined by variations in grain size, fabric, and the presence of localized slip surfaces. In the present set of experiments, the microstructural domains and the principal slip zone varied in thickness at different slip rates (Fig. 7). In Figure 8, the thickness of the principal slip zone has been tracked at different deformation conditions (i.e. slip rate and presence of water).



180 3.5.1 Microstructures of room humidity experiments

At slip rates $\leq 0.01 \text{ ms}^{-1}$, gouges were characterized by the development of a 500-900 μm thick slip zone (Fig. 9a), consisting of a fine-grained matrix (grain size c. 1 μm) containing subrounded grains of dolomite c. 5-10 μm in size (Fig. 9b). The slip zone contains sub-parallel, 10-30 μm thick Y, R, and R_1 type shear bands (using the terminology of Logan et al., 1979, Fig. 9a,c). Each individual shear band is associated with a very fine-grained matrix (grain size $< 1 \mu\text{m}$) composed of calcite and dolomite.
185 The presence of multiple interlinked shear bands contributes to a weak foliation within the slip zone that lies sub-parallel to gouge layer boundaries (Fig. 9a). Y-, R-, and most notably R_1 -shears, gradually decrease in abundance with increasing slip rate. The transition from fine-grained slip zone to highly fractured bulk gouge is typically well-defined (see upper part in Fig. 9d). The bulk gouge shows widespread cataclasis and intragranular fracturing, which is focussed preferentially into calcite grains (Smith et al., 2017; Demurtas et al., 2019a). Fractures that cut relatively large grains of calcite in the bulk gouge often
190 exploit cleavage planes (e.g. Fig. 9d; Smith et al., 2017; Demurtas et al., 2019a).

At a slip rate of 0.1 ms^{-1} , the bulk gouge develops a weak foliation defined by compositional banding of heavily fractured calcite- and dolomite-rich domains, which lie adjacent to a localized principal slip zone c. 110 μm thick (Fig. 9e). The foliation is inclined $25\text{-}30^\circ$ to the principal slip surface and appears to form by disaggregation and shearing of originally intact calcite and dolomite grains (Fig. 9e). Locally, the principal slip surface is associated with discontinuous lens-shaped patches (up to
195 15-20 μm thick) of calcite with irregular boundaries and negligible porosity (Fig. 9f).

In experiments conducted at 1 ms^{-1} , the bulk gouges developed a well-defined foliation across most of the thickness of the layers (Smith et al., 2017; Demurtas et al., 2019a, b). The foliation is defined by alternating calcite- and dolomite-rich domains inclined at c. 40° to the principal slip surface (Fig. 10a-b), which become progressively rotated as they approach the slip surface (Fig. 10c). Large remnant grains (up to 200 μm) in the bulk gouge are often rimmed by fractured tails of finer-
200 grained aggregates (grain size $< 10 \mu\text{m}$), and resemble mantled porphyroclasts in mylonites (e.g. Snoke et al., 1998; Trouw and Passchier, 2009) (arrow in Fig. 10a). At distances of $< 400 \mu\text{m}$ from the principal slip surface, the mean grain size decreases substantially, there are very few large surviving grains (up to c. 100 μm in size), and there is a greater degree of mixing between calcite and dolomite (see more uniform colouring in the upper part of EDS map in Fig. 10b). The principal slip zone consists of a 15-20 μm thick, extremely fine-grained layer ($\ll 1 \mu\text{m}$ in size) composed of calcite, Mg-calcite, dolomite, and
205 periclase (EDS and XRPD analysis; Figs. 6 and 10c-d). Calcite forms elongate aggregates with negligible porosity that display an aggregate preferred orientation with the long axes sub-parallel to foliation (Fig. 10c-e). Dolomite-rich domains show higher porosity and preserve distinct grain structures (Fig. 10c-d). EBSD analysis of elongate calcite aggregates within the principal slip zone (Fig. 10e) shows a distinct crystallographic preferred orientation with c-axes inclined sub-perpendicular to gouge layer boundaries (Fig. 10f; see also Demurtas et al., 2019b). Adjacent to the principal slip zone, a c. 30-40 μm thick layer
210 includes dolomite grains with diffuse internal cracking, clusters of small holes, and vesicular rims previously interpreted as resulting from degassing during decarbonation of comminuted dolomite grains (Fig. 10c; Mitchell et al., 2015; Demurtas et al., 2019b). At 1 ms^{-1} and 26 MPa, the foliation was found only within 400 μm of the principal slip surface (Supplementary



Material). The principal slip zone was composed of a calcite-rich recrystallized layer, with substantially reduced porosity and well-rounded dolomite clasts a few micrometres in size (Supplementary Material).

215 3.5.2 Microstructures of water-dampened experiments

In the bulk gouges, the region furthest from the slip zone is composed of grains that show very limited fracturing and resemble the starting materials (Fig. 11a,d; compare with Fig. 1e). Towards the slip zone, grains are increasingly fractured and become rounder. As in the room humidity experiments, most of the larger “surviving” grains are composed of dolomite (Fig. 11e), consistent with data showing that calcite undergoes more efficient grain size reduction compared to dolomite (Smith et al., 2017; 220 Demurtas et al., 2019a). Domain boundaries (e.g. between intact bulk gouge and comminuted gouge) are often gradational (Fig. 11d), and the total thickness of the comminuted zone is observed to decrease at higher slip rates (from c. 1500 μm thick at 30 μms^{-1} to c. 150 μm thick at 1 ms^{-1}). The principal slip zone consists of an ultrafine-grained matrix (grain size $<1 \mu\text{m}$) composed of a mixture of calcite and dolomite, with a few well-rounded surviving dolomite grains up to 20–30 μm in size (Fig. 11b–c). At the lowest slip rate (i.e. 30 μms^{-1}), the principal slip zone has a sharp boundary with a characteristic wavelength 225 with the underlying gouge (Fig. 11d), and contains irregular flame-like structures defined by subtle variations in the content of calcite and dolomite (Fig. 11b). The principal slip zone is cut by discrete slip surfaces oriented subparallel to the boundaries of the gouge (Y-shear, Fig. 11c). Experiments performed at 30 μms^{-1} with increasing displacement (*s1327*, *s1329*, *s1328*, *s1330-s1214* with displacement of 0.05–0.1–0.2–0.4 m, respectively; Table 1) show that the three distinct microstructural domains are already recognizable after <0.05 m of slip (Fig. 11d), and that the final thickness of each microstructural domain is a function 230 of total slip and slip rate. At a slip rate of 0.1 ms^{-1} , the comminuted principal slip zone shows distinct grain-size grading, characterized by an abundance of relatively large and angular dolomite particles towards the stationary side of the slip zone, and an absence of such particles towards the rotary side (Fig. 11e). Measurements of the thickness of the principal slip zone at different slip rates (Fig. 8) show a log-linear decrease in thickness from c. 400 μm at 30 μms^{-1} to c. 30 μm at 1 ms^{-1} .

At a slip rate of 1 ms^{-1} , the gouge contains an intensely comminuted c. 300–400 μm thick layer bordering the principal slip 235 zone (Fig. 11f). The transition between the two domains is sharp and characterized in places by the occurrence of discrete Y-shears. The principal slip zone consists of lens-shaped patches of a calcite-rich and fine-grained (grain size $<1 \mu\text{m}$) layer c. 30 μm thick with negligible porosity, which is embedded in a highly comminuted and fine-grained matrix containing a few larger dolomite grains. The principal slip surface cuts sharply through this layer and truncates larger clasts (Fig. 11f–g). Locally, reworked angular fragments of the principal slip zone are found (Fig. 11h).

240 4 Discussion

4.1 Microstructural evolution and weakening mechanisms in calcite-dolomite mixtures

The mechanical behaviour and microstructural evolution of calcite-dolomite gouges show substantial differences based on the availability of water during deformation. In room humidity conditions, slip strengthening at slip rates $\leq 0.01 \text{ms}^{-1}$ is associated



with (i) initial compaction followed by dilation (Fig. 4a) and (ii) the development of a $>500 \mu\text{m}$ thick slip zone composed of a
245 fine-grained ($c. 1 \mu\text{m}$) calcite-dolomite mixture cut by Y-, R-, and R_1 -shear bands (Fig. 9). These observations have previously
been interpreted to relate to the development and broadening of a distributed zone of deformation during strain hardening (e.g.
Marone et al., 1990; Beeler et al., 1996; Rathbun and Marone, 2010). This is also supported by widening of the main peaks
for calcite and dolomite in XRPD analysis (Fig. 6a), which is interpreted to result from a decrease in the mean crystallite size
or deformation-induced microstrain within the crystallites (e.g. Ungár, 2004). A much shorter initial period of dilatancy is
250 observed in experiments performed at $V \geq 0.1 \text{ ms}^{-1}$ (Fig. 4a), and this correlates with (i) a transition from slip hardening to
slip weakening (Figs. 2-3) and (ii) the development of a well-defined, localized principal slip zone that accommodates most of
the strain after it forms (Figs. 9e-f and 10) (see also Han et al., 2007; Fondriest et al., 2013; Smith et al., 2013, 2015; Green
et al., 2015; De Paola et al., 2015; Mitchell et al., 2015; Rempe et al., 2017; Pozzi et al., 2019; Demurtas et al., 2019b). The
switch to slip weakening friction and a higher degree of strain localization is also accompanied by a significant temperature
255 rise generated within the principal slip zone (Fig. 5a), CO_2 emissions (Fig. 5b), and the formation of Mg-calcite and periclase
in samples collected from the principal slip zone (Fig. 6c). Collectively, these observations suggest that the temperature rise at
relatively high slip velocities caused dynamic weakening and decarbonation of dolomite (and possibly calcite).

At high slip rates ($V \geq 0.1 \text{ ms}^{-1}$), the onset of dynamic weakening in carbonate gouges deformed at room humidity has
been interpreted as a consequence of local heating along incipient slip surfaces, which eventually coalesce into a localized
260 and through-going shear band (De Paola et al., 2015; Smith et al., 2015; Rempe et al., 2017). Further slip then increases
the bulk temperature due to continued frictional heating in the principal slip zone and dissipation of heat in to the bulk gouge,
resulting in local gouge recrystallization (Smith et al., 2015). Under these conditions, high strain rates can be accommodated by
temperature- and grain size-dependent deformation mechanisms leading to “viscous” flow (Green et al., 2015; De Paola et al.,
2015; Pozzi et al., 2018, 2019; Demurtas et al., 2019b). Demurtas et al. (2019b) performed Transmission Kikuchi Diffraction
265 (TKD) analysis on electron-transparent samples of the low porosity, fine-grained principal slip zone of experiment *s1221* ($V =$
 1 ms^{-1} under room humidity conditions; Fig. 10c) to investigate the deformation mechanisms active during coseismic sliding in
calcite-dolomite mixtures. Their results show that the principal slip zone is composed of a nanogranular aggregate made of two
grain populations: (i) nanograins 100-300 nm in size exhibiting low internal lattice distortion, compatible with deformation
by grain size sensitive creep, and (ii) nanograins $>800 \text{ nm}$ in size showing development of subgrains, suggesting deformation
270 by grain size insensitive creep (Demurtas et al., 2019b). Although the maximum temperature measured during deformation
in the present experiments was $621 \text{ }^\circ\text{C}$ (Fig. 5a), accommodation of the calculated strain rates ($\dot{\gamma} = 6 \times 10^3 \text{ s}^{-1}$) could be
explained by the significant decrease of the activation energy for creep mechanisms (but also decarbonation reactions) due to
the nanogranular nature of the particles (Demurtas et al., 2019b). Similar observations have been documented by Pozzi et al.
(2019) in experimental nanogranular principal slip zones in pure calcite gouges deformed at coseismic slip rates. Alternatively,
275 the temperatures achieved in the slip zones of high velocity ($V = 1 \text{ ms}^{-1}$) but short duration experiments ($<0.5 \text{ s}$) could be higher
than those measured with thermocouples and estimated using numerical models. The thermocouples used here were located a
few mm from the edge of the slipping zone (Fig. 1b). Additionally, they have large thermal inertia and low real acquisition rates
because the electric potential developing in response to temperature changes is very slow (0.1-0.5 s) compared to the duration



of the experiments (c. 0.5 s) (Sarnes and Schrüfer, 2007). Recent studies in which the temperature during experimental seismic
280 slip was measured with optical fibres located inside the slip zone (in-situ measurements at acquisition rates of 1 kHz) detected
temperatures 300-400 °C higher than those measured with thermocouples (Aretusini et al., 2019). Temperatures in the slipping
zone substantially higher than 621 °C would make grain size- and temperature-dependent deformation mechanisms more
efficient. Instead, in the case of experiment *s1218* performed at $V = 0.1 \text{ ms}^{-1}$, the moderate dynamic weakening ($\mu_{ss} = 0.55$)
can be related to more limited frictional heating within the principal slip zone both in time (max temperature measured of
285 190 °C, Fig. 5a) and space (patchy recrystallized areas in Fig. 9e-f). However, at least locally, the temperature increase was
sufficiently large to decompose dolomite, as testified by the clear CO₂ peak measured during shearing at this velocity (Fig. 5b).

In water-dampened conditions, the mechanical behaviour of the calcite-dolomite mixtures is similar (slight slip strengthening
to slip neutral) at all slip rates up to 0.1 ms^{-1} (Fig. 2c). The thickness of the principal slip zone decreases log-linearly with
increasing slip rate, indicating a progressively higher degree of localization (Fig. 8). However, this has no obvious effect on
290 the steady state friction coefficient (Fig. 3b), possibly suggesting that the steady state is controlled by strain and that strain is
kept constant by microstructural reorganization distributed within the slip zone. The principal slip zone is composed of a very
fine-grained ($\ll 1 \mu\text{m}$) matrix of calcite and dolomite that includes a few well-rounded dolomite clasts up to 20-30 μm in size
(Fig. 11). The similarity in microstructure at all investigated slip rates suggests that water has a major role in promoting faster
grain size reduction at the onset of slip, possibly by decreasing the surface energy and yield stress of calcite and dolomite
295 (Risnes et al., 2005; Røyne et al., 2011). XRPD analysis of the slip surface of experiment *s1214* ($30 \mu\text{ms}^{-1}$) showed the
formation of aragonite (Fig. 6b). Given that the starting materials were composed of calcite and dolomite only, the aragonite
must have formed during deformation. Li et al. (2014), documented polymorphic transformation of calcite into aragonite due to
mechanical grinding in a dry (i.e. room humidity) environment. Our observations therefore suggest that relatively dry patches
could develop in the gouge layer during slip (or were present at the onset of slip), or that such transformation is also possible
300 under water saturated conditions.

The slip zone of the water-dampened experiment performed at $30 \mu\text{ms}^{-1}$ is characterized by flame-like structures, and domain
boundaries that display a characteristic wavelength (Fig. 11b,d). Similar structures are typical of soft sediment deformation
(Allen, 1985) and have also been described within fault cores (Brodsky et al., 2009), where they are interpreted to result from
fluid mobilization and a difference in viscosity between two adjacent layers during deformation. Additionally, the occurrence
305 of grain size grading within the water-dampened principal slip zone formed at a slip rate of 0.1 ms^{-1} is indicative of grain
rearrangement due to frictional sliding (see Masoch et al., 2019, and reference therein), referred to as the “Brazil nut” effect, a
phenomenon observed when large grains move to the top of a fluidized layer due to differences in dispersal pressure between
large and small particles (Williams, 1976). Grain size grading was reported by Boullier et al. (2009) from the principal slip
zone of the 1999 M_w 7.6 Chi-Chi earthquake in Taiwan, and from exhumed normal faults in Alpine Corsica (Masoch et al.,
310 2019). Additionally, similar microstructures were produced by Boulton et al. (2017) in high velocity rotary-shear experiments
($V = 1 \text{ ms}^{-1}$) performed on clay-rich drill chips retrieved from the Alpine Fault (New Zealand). As in the experiments by
Boulton et al. (2017), grain size grading in our experiments was observed only in water-dampened conditions. Collectively,
the presence of flame-like structures, undulating domain boundaries with a characteristic wavelength, and grain-size grading,



suggests that water-dampened gouges experienced fluidization at slip rates between $30 \mu\text{ms}^{-1}$ and 0.1ms^{-1} . This is significant
315 because textures related to fluidization in natural gouges and cataclasites are often interpreted to form during coseismic slip at
high velocities (e.g. Monzawa and Otsuki, 2003; Rowe et al., 2005; Boullier et al., 2009; Brodsky et al., 2009; Demurtas et
al., 2016; Boulton et al., 2017; Smeraglia et al., 2017). Various mechanisms have been proposed to account for fluidization of
granular materials in fault zones, including (i) frictional heating and thermal pressurization (Boullier et al., 2009), (ii) dilation
that limits grain-grain contacts (Borradaile, 1981; Monzawa and Otsuki, 2003), and (iii) focussed fluid flow along slip zones
320 during and after coseismic sliding (e.g. fault-valve mechanism of Sibson, 1990). In our experiments, temperature measurements
made during slip at $30 \mu\text{ms}^{-1}$ suggest that significant frictional heating is unlikely, and therefore thermal pressurization is an
unlikely mechanism within the slip zone. Water-dampened experiments are characterized by continuous compaction, which
also excludes the dilation-related hypothesis of Borradaile (1981). We propose that fluidization in the principal slip zone might
be caused by local fluid pressure increase within water-saturated patches as a result of continuous compaction combined with
325 minimal fluid loss during deformation. A sudden release of water from the pressurized patch could result in gouge mobilization
and injection of material in to the adjacent slip zone.

In water-dampened experiments at 1ms^{-1} , abrupt dynamic weakening preceded by a very short-lived strengthening phase has
previously been documented in experiments on calcite gouges (Rempe et al., 2017) and calcite marbles (Violay et al., 2014). In
gouges, Rempe et al. (2017) suggested that the rapid onset of dynamic weakening could be related to faster grain size reduction
330 in the presence of water, leading to an early switch from brittle deformation to grain size sensitive creep in the principal slip
zone, analogous to the process suggested to occur in dry gouges (De Paola et al., 2015; Demurtas et al., 2019b; Pozzi et al.,
2019). However, there is an apparent discrepancy between the relatively low maximum temperature measured close to the
principal slip zone in water-dampened experiments ($200 \text{ }^\circ\text{C}$ at $V = 1 \text{ms}^{-1}$; Fig. 5a), and the observed CO_2 production (Fig.
5b) combined with microstructural evidence for recrystallization during deformation (Fig. 11f-g). As previously discussed, this
335 could be due to an underestimate of peak temperature (Aretusini et al., 2019). Alternatively, Ohl et al. (2020) proposed that
mechanical liming (see Martinelli and Plescia, 2004) along natural faults could be a possible slip weakening mechanism that
does not necessarily involve a macroscopic temperature increase of $>500\text{-}600 \text{ }^\circ\text{C}$.

4.2 Foliation development in calcite-dolomite gouges at coseismic slip rates

Foliated gouges and cataclasites are common fault rocks in the brittle upper crust (Snoke et al., 1998). Typically, they are
340 interpreted to form due to a combination of cataclasis and dissolution-precipitation reactions during aseismic fault creep (e.g.
Rutter et al., 1986; Chester and Chester, 1998; Lin, 2001; Collettini and Holdsworth, 2004; Jefferies et al., 2006; De Paola et
al., 2008; Wallis et al., 2013). Experimental observations support this idea, and show that well-defined foliations can form as a
result of dissolution-precipitation reactions accompanied by granular flow and frictional sliding at low slip rates ($V < 1 \mu\text{ms}^{-1}$;
Bos et al., 2000; Niemeijer and Spiers, 2006).

345 However, the association of foliated fault rocks with possible microstructural indicators of seismic slip in natural fault
rocks (e.g. mirror-like slip surfaces with truncated clasts, see Demurtas et al., 2016) led Smith et al. (2017) to investigate the
possibility that some foliated gouges and cataclasites might have a coseismic origin. Rotary-shear experiments performed at



a slip rate of 1.13 ms^{-1} on gouges composed of 50 wt.% calcite and 50 wt.% dolomite showed the development of a foliation defined by an organized banding of heavily fractured calcite and dolomite clasts (Smith et al., 2017). Experiments performed at increasing displacements revealed that the foliations are established during the initial strengthening phase, when distributed strain throughout the bulk gouge causes grain comminution and distributed shearing. Once dynamic weakening occurs, strain progressively localizes into a single continuous principal slip zone, and the foliation in the bulk gouge does not show any further microstructural change. Shear strain analysis of the foliated layers showed that relatively low values of strain ($\gamma < 4$) are needed to develop a foliation. Based on their observations, Smith et al. (2017) suggested that some natural foliated gouges and cataclasites characterized by compositional banding, grain size variations, and preferred particle or fracture alignments, could form by distributed brittle flow as strain localizes during coseismic shearing, especially if such foliations are found in proximity to microstructural indicators of coseismic slip. The experiments presented in this paper allow us to test this hypothesis over a wider range of slip rates (i.e. $30 \mu\text{ms}^{-1} - 1 \text{ ms}^{-1}$) and deformation conditions (i.e. room humidity vs. water dampened). The formation of well-defined foliations throughout the bulk gouge was only observed at high slip rates ($V = 1 \text{ ms}^{-1}$) and room humidity conditions (Fig. 10), corresponding to the conditions presented in Smith et al. (2017). Local foliation development was also observed in lower velocity experiments at room humidity, although this was restricted to regions $<400 \mu\text{m}$ from the principal slip surface (Fig. 9e).

Our new experiments support the hypothesis presented in Smith et al. (2017) that well-defined foliations in calcite-dolomite gouges can form during high velocity sliding in carbonate gouges, and could be used in conjunction with other microstructures (e.g. seismic slip indicators) to better understand localization processes in faults. The lowest slip velocity studied here (i.e. $30 \mu\text{ms}^{-1}$) is still too high for pressure-solution to be efficient in calcite or dolomite. Lower slip rates might promote the activation of pressure-solution, which could result in the formation of a foliation under certain conditions. Grain elongation and foliation development have previously been reported in experiments performed on calcite-dolomite mixtures by Delle Piane et al. (2009). However, in this case, the deformation conditions (i.e. torsion experiments at temperatures of $700\text{--}800 \text{ }^\circ\text{C}$, confining pressure of 300 MPa , shear strain rate of $3 \times 10^{-4/5} \text{ s}^{-1}$) were representative of mid- to lower crustal depths, rather than the low-pressure low-temperature ambient conditions explored here.

5 Conclusions

A series of rotary-shear experiments was performed on gouges composed of 50 wt.% calcite and 50 wt.% dolomite to develop an understanding of microstructural evolution at a range of slip rates ($30 \mu\text{ms}^{-1} - 1 \text{ ms}^{-1}$), fluid conditions (room humidity and water dampened), total displacements (0.05–0.4 m), and normal loads (17.5 and 26 MPa).

The evolution of the apparent friction coefficient is strongly influenced by the presence of water: at room humidity, slip strengthening is observed up to slip rates of 0.01 ms^{-1} , above which dynamic weakening occurs. In water-dampened conditions, slight slip strengthening to slip neutral friction characterises experiments up to slip velocities of 0.1 ms^{-1} , above which dynamic weakening occurs abruptly. The mechanical differences observed under room humidity and water-dampened conditions are also reflected in the microstructures of the deformed gouge layers. At room humidity, slip strengthening is associated with



diffuse deformation and the development of a relatively thick slip zone cut by Y-, R-, and R₁-shear bands. The onset of dynamic weakening is concomitant with the development of a localised principal slip zone containing evidence of dolomite decarbonation and calcite recrystallization. In the presence of water, evidence of gouge fluidization within a fine-grained principal slip zone is observed at slip rates from 30 μms^{-1} to 0.1 ms^{-1} , suggesting that fluidization may not be restricted to
385 coseismic slip rates. At 1 ms^{-1} , the principal slip zone is characterised by patches of recrystallized calcite that are locally broken and reworked.

The development of a well-defined foliation in the bulk gouge layer only occurs in room humidity experiments at a slip rate of 1 ms^{-1} , consistent with the work of Smith et al. (2017). This observation supports the notion that some foliated gouges and cataclasites may form during coseismic slip in natural carbonate-bearing faults.

390 *Data availability.* Mechanical data from the experiments are available upon request from the corresponding author.

Author contributions. MD, SAFS, ES and GDT designed the project. MD and ES performed the experiments. MD and SAFS performed the microstructural analysis. MD, SAFS, ES and GDT were part of the discussion and contributed to the writing of the manuscript.

Competing interests. The authors declare that they have no conflict of interest.

Acknowledgements. MD, ES and GDT were supported by the European Research Council Consolidator grant project 614705 NOFEAR.
395 SAFS acknowledges the Marsden Fund Council (projects UOO1417 and UOO1829) administered by the Royal Society of New Zealand. Stefano Aretusini and Michele Fondriest are thanked for fruitful discussions. Marianne Negrini provided assistance with the SEM at the Otago Centre for Electron Microscopy, University of Otago. Federico Zorzi is thanked for performing the XRPD analysis and Leonardo Tauro for assistance during thin section preparation.



References

- 400 Allen, J.R.L.: Principles of Physical Sedimentology, George Allen and Unwin, Boston, 272 pp, 1985.
- Aretusini S., Nuñez Cascajero, A., Spagnuolo, E., Tapetado, A., Vazquez, C., Di Toro, G.: How hot is a lab-earthquake? American Geophysical Union Fall Meeting Abstract 519812, M23E-0160, San Francisco (USA), 2019.
- Austin, N. J. and Kennedy, L. A.: Textural controls on the brittle deformation of dolomite: Variations in peak strength, in Deformation Mechanisms, Rheology and Tectonics: from Minerals to the Lithosphere, vol. 243, edited by D. Gapais, J. P. Brun, and P. R. Cobbold, pp. 405 37–49, Geological Society, London, Special Publications., 2005.
- Barber, D. J., Heard, H. C. and Wenk, H. R.: Deformation of dolomite single crystals from 20–800 °C, *Phys. Chem. Miner.*, 7(6), 271–286, doi:10.1007/BF00311980, 1981.
- Beeler, N. M., Tullis, T. E., Blanpied, M. L. and Weeks, J. D.: Frictional behavior of large displacement experimental faults, *J. Geophys. Res. Solid Earth*, 101(B4), 8697–8715, doi:10.1029/96JB00411, 1996.
- 410 Bestmann, M., Kunze, K. and Matthews, A.: Evolution of a calcite marble shear zone complex on Thassos Island, Greece: Microstructural and textural fabrics and their kinematic significance, *J. Struct. Geol.*, 22(11–12), 1789–1807, doi:10.1016/S0191-8141(00)00112-7, 2000.
- Bestmann, M., Prior, D. J. and Grasemann, B.: Characterisation of deformation and flow mechanics around porphyroclasts in a calcite marble ultramylonite by means of EBSD analysis, *Tectonophysics*, 413(3–4), 185–200, doi:10.1016/j.tecto.2005.10.044, 2006.
- Brodsky, E. E., Rowe, C. D., Meneghini, F. and Moore, J. C.: A geological fingerprint of low-viscosity fault fluids mobilized during an 415 earthquake, *J. Geophys. Res. Solid Earth*, 114(1), 1–14, doi:10.1029/2008JB005633, 2009.
- Borradaile, G. J.: Particulate flow of rock and the formation of cleavage, *Tectonophysics*, 72(3–4), 305–321, doi:10.1016/0040-1951(81)90243-2, 1981.
- Bos, B., Peach, C. J. and Spiers, C. J.: Frictional-viscous flow of simulated fault gouge caused by the combined effects of phyllosilicates and pressure solution, *Tectonophysics*, 327, 173–194, 2000.
- 420 Boullier, A. M., Yeh, E. C., Boutareaud, S., Song, S. R. and Tsai, C. H.: Microscale anatomy of the 1999 Chi-Chi earthquake fault zone, *Geochemistry, Geophys. Geosystems*, 10(3), doi:10.1029/2008GC002252, 2009.
- Boulton, C., Yao, L., Faulkner, D. R., Townend, J., Toy, V. G., Sutherland, R., Ma, S. and Shimamoto, T.: High-velocity frictional properties of Alpine Fault rocks: Mechanical data, microstructural analysis, and implications for rupture propagation, *J. Struct. Geol.*, 97, 71–92, doi:10.1016/j.jsg.2017.02.003, 2017.
- 425 Busch, J. P. and van der Pluijm, B. A.: Calcite textures, microstructures and rheological properties of marble mylonites in the Bancroft shear zone, Ontario, Canada, *J. Struct. Geol.*, 17(5), 677–688, doi:10.1016/0191-8141(94)00092-E, 1995.
- Chester, F. M. and Chester, J. S.: Ultracataclasite structure and friction processes of the Punchbowl fault, San Andreas system, California, *Tectonophysics*, 295(1–2), 199–221, doi:10.1016/S0040-1951(98)00121-8, 1998.
- Collettini, C. and Holdsworth, R. E.: Fault zone weakening and character of slip along low-angle normal faults: Insights from the Zuccale 430 fault, Elba, Italy, *J. Geol. Soc. London.*, 161(6), 1039–1051, doi:10.1144/0016-764903-179, 2004.
- Davis, N. E., Kronenberg, A. K. and Newman, J.: Plasticity and diffusion creep of dolomite, *Tectonophysics*, 456(3–4), 127–146, doi:10.1016/j.tecto.2008.02.002, 2008.
- De Bresser, J. H. P. and Spiers, C. J.: High-temperature deformation of calcite single crystals by r+ and f+ slip, in Geological Society Special Publication, vol. 54, edited by R. J. Knipe and E. H. Rutter, pp. 285–298, Geological Society Special Publication., 1990.



- 435 De Paola, N., Mirabella, F., Barchi, M. R. and Burchielli, F.: Early orogenic normal faults and their reactivation during thrust belt evolution: the Gubbio Fault case study, Umbria-Marche Apennines (Italy), *J. Struct. Geol.*, 28(11), 1948–1957, doi:10.1016/j.jsg.2006.06.002, 2006.
- De Paola, N., Collettini, C., Faulkner, D. R. and Trippetta, F.: Fault zone architecture and deformation processes within evaporitic rocks in the upper crust, *Tectonics*, 27(4), 1–21, doi:10.1029/2007TC002230, 2008.
- De Paola, N., Chiadini, G., Hirose, T., Cardellini, C., Caliro, S. and Shimamoto, T.: The geochemical signature caused by earthquake
440 propagation in carbonate-hosted faults, *Earth Planet. Sci. Lett.*, 310(3–4), 225–232, doi:10.1016/j.epsl.2011.09.001, 2011a.
- De Paola, N., Hirose, T., Mitchell, T., Di Toro, G., Viti, C. and Shimamoto, T.: Fault lubrication and earthquake propagation in thermally unstable rocks, *Geology*, 39(1), 35–38, doi:10.1130/G31398.1, 2011b.
- De Paola, N., Holdsworth, R. E., Viti, C., Collettini, C. and Bullock, R.: Can grain size sensitive flow lubricate faults during the initial stages of earthquake propagation?, *Earth Planet. Sci. Lett.*, 431, 48–58, doi:10.1016/j.epsl.2015.09.002, 2015.
- 445 Delle Piane, C., Burlini, L. and Grobety, B.: Reaction-induced strain localization: Torsion experiments on dolomite, *Earth Planet. Sci. Lett.*, 256(1–2), 36–46, doi:10.1016/j.epsl.2007.01.012, 2007.
- Delle Piane, C., Burlini, L., Kunze, K., Brack, P. and Burg, J. P.: Rheology of dolomite: Large strain torsion experiments and natural examples, *J. Struct. Geol.*, 30(6), 767–776, doi:10.1016/j.jsg.2008.02.018, 2008.
- Delle Piane, C., Burlini, L. and Kunze, K.: The influence of dolomite on the plastic flow of calcite. Rheological, microstructural and chemical
450 evolution during large strain torsion experiments, *Tectonophysics*, 467(1–4), 145–166, doi:10.1016/j.tecto.2008.12.022, 2009.
- Delle Piane, C., Clennell, M. Ben, Keller, J. V. A., Giwelli, A. and Luzin, V.: Carbonate hosted fault rocks: A review of structural and microstructural characteristic with implications for seismicity in the upper crust, *J. Struct. Geol.*, 103, 17–36, doi:10.1016/j.jsg.2017.09.003, 2017.
- Demurtas, M., Fondriest, M., Balsamo, F., Clemenzi, L., Storti, F., Bistacchi, A. and Di Toro, G.: Structure of a normal seismogenic
455 fault zone in carbonates: The Vado di Corno Fault, Campo Imperatore, Central Apennines (Italy), *J. Struct. Geol.*, 90, 185–206, doi:10.1016/j.jsg.2016.08.004, 2016.
- Demurtas, M., Smith, S. A. F., Prior, D. J., Spagnuolo, E. and Di Toro, G.: Development of crystallographic preferred orientation during cataclasis in low-temperature carbonate fault gouge, *J. Struct. Geol.*, 126(May), 37–50, doi:10.1016/j.jsg.2019.04.015, 2019a.
- Demurtas, M., Smith, S. A. F., Prior, D. J., Brenker, F. E. and Di Toro, G.: Grain size sensitive creep during simulated seismic
460 slip in nanogranular fault gouges: constraints from Transmission Kikuchi Diffraction (TKD), *J. Geophys. Res. Solid Earth*, 124, doi:10.1029/2019jb018071, 2019b.
- Di Toro, G., Niemeijer, A. R., Tripoli, A., Nielsen, S., Di Felice, F., Scarlato, P., Spada, G., Alessandrini, R., Romeo, G., Di Stefano, G., Smith, S., Spagnuolo, E. and Mariano, S.: From field geology to earthquake simulation: A new state-of-the-art tool to investigate rock friction during the seismic cycle (SHIVA), *Rend. Lincei*, 21(SUPPL. 1), 95–114, doi:10.1007/s12210-010-0097-x, 2010.
- 465 Fondriest, M., Smith, S. A. F., Candela, T., Nielsen, S. B., Mair, K. and Toro, G. Di: Mirror-like faults and power dissipation during earthquakes, *Geology*, 41(11), 1175–1178, doi:10.1130/G34641.1, 2013.
- Fondriest, M., Aretusini, S., Di Toro, G. and Smith, S. A. F.: Fracturing and rock pulverization along an exhumed seismogenic fault zone in dolostones: The Foiana Fault Zone (Southern Alps, Italy), *Tectonophysics*, 654, 56–74, doi:10.1016/j.tecto.2015.04.015, 2015.
- Fondriest, M., Balsamo, F., Bistacchi, A., Clemenzi, L., Demurtas, M., Storti, F. and Di Toro, G.: Structural Complexity and Mechanics of a
470 Shallow Crustal Seismogenic Source (Vado di Corno Fault Zone, Italy), *J. Geophys. Res. Solid Earth*, 125(9), doi:10.1029/2019jb018926, 2020.



- Green II, H. W., Shi, F., Bozhilov, K., Xia, G. and Reches, Z.: Phase transformation and nanometric flow cause extreme weakening during fault slip, *Nat. Geosci.*, 8(6), 484–489, doi:10.1038/ngeo2436, 2015.
- Han, R., Shimamoto, T., Ando, J. and Ree, J.-H.: Seismic slip record in carbonate-bearing fault zones: An insight from high-velocity friction experiments on siderite gouge, *Geology*, 35(12), 1131–1134, doi:10.1130/G24106A.1, 2007.
- 475 Holyoke, C. W., Kronenberg, A. K. and Newman, J.: Microstructural evolution during strain localization in dolomite aggregates, *J. Struct. Geol.*, 69(PB), 449–464, doi:10.1016/j.jsg.2014.04.008, 2014.
- Jefferies, S. P., Holdsworth, R. E., Shimamoto, T., Takagi, H., Lloyd, G. E. and Spiers, C. J.: Origin and mechanical significance of foliated cataclastic rocks in the cores of crustal-scale faults: Examples from the Median Tectonic Line, Japan, *J. Geophys. Res. Solid Earth*, 480 111(12), 1–17, doi:10.1029/2005JB004205, 2006.
- Kennedy, L. A. and Logan, J. M.: The role of veining and dissolution in the evolution of fine-grained mylonites: the McConnell thrust, Alberta, *J. Struct. Geol.*, 19(6), 785–797, doi:10.1016/S0191-8141(97)00005-9, 1997.
- Kennedy, L. A. and White, J. C.: Low-temperature recrystallization in calcite: Mechanisms and consequences, *Geology*, 29(11), 1027–1030, doi:10.1130/0091-7613(2001)029<1027:LTRICM>2.0.CO, 2001.
- 485 Kitajima, H., Chester, J. S., Chester, F. M. and Shimamoto, T.: High-speed friction of disaggregated ultracataclasite in rotary shear: Characterization of frictional heating, mechanical behavior, and microstructure evolution, *J. Geophys. Res. Solid Earth*, 115(8), 1–21, doi:10.1029/2009JB007038, 2010.
- Kushnir, A. R. L., Kennedy, L. A., Misra, S., Benson, P. and White, J. C.: The mechanical and microstructural behaviour of calcite-dolomite composites: An experimental investigation, *J. Struct. Geol.*, 70, 200–216, doi:10.1016/j.jsg.2014.12.006, 2015.
- 490 Li, T., Sui, F., Li, F., Cai, Y. and Jin, Z.: Effects of dry grinding on the structure and granularity of calcite and its polymorphic transformation into aragonite, *Powder Technol.*, 254, 338–343, doi:10.1016/j.powtec.2014.01.043, 2014.
- Lin, A.: S-C fabrics developed in cataclastic rocks from the Nojima fault zone, Japan and their implications for tectonic history, *J. Struct. Geol.*, 23(6–7), 1167–1178, doi:10.1016/S0191-8141(00)00171-1, 2001.
- Liu, J., Walter, J. M. and Weber, K.: Fluid-enhanced low-temperature plasticity of calcite marble: Microstructures and mechanisms, *Geology*, 495 30(9), 787–790, doi:10.1130/0091-7613(2002)030<0787:FELTPO>2.0.CO;2, 2002.
- Logan, J. M., M. Friedman, N. Higgs, C. Dengo, and T. Shimamoto: Experimental studies of simulated gouge and their application to studies of natural fault zones, *Proceedings of Conference VIII on Analysis of Actual Fault Zones in Bedrock*, U.S. Geological Survey Open-File Report 79–1239, 1979.
- Marone, C., Raleigh, C. B. and Scholz, C. H.: Frictional behavior and constitutive modeling of simulated fault gouge, *J. Geophys. Res.*, 500 95(B5), 7007–7025, 1990.
- Martinelli, G. and Plescia, P.: Mechanochemical dissociation of calcium carbonate: Laboratory data and relation to natural emissions of CO₂, *Phys. Earth Planet. Inter.*, 142(3–4), 205–214, doi:10.1016/j.pepi.2003.12.009, 2004.
- Masoch, S., Fondriest, M., Preto, N., Secco, M. and Di Toro, G.: Seismic cycle recorded in cockade-bearing faults (Col de Teghime, Alpine Corsica), *J. Struct. Geol.*, 129(August), 103889, doi:10.1016/j.jsg.2019.103889, 2019.
- 505 Miller, J. A., Viola, G. and Mancktelow, N. S.: Oxygen, carbon and strontium isotope constraints on the mechanisms of nappe emplacement and fluid-rock interaction along the subhorizontal Naukluft Thrust, central Namibia, *J. Geol. Soc. London.*, 165(3), 739–753, doi:10.1144/0016-76492007-079, 2008.



- Mitchell, T. M., Smith, S. A. F., Anders, M. H., Di Toro, G., Nielsen, S., Cavallo, A. and Beard, A. D.: Catastrophic emplacement of giant landslides aided by thermal decomposition: Heart Mountain, Wyoming, *Earth Planet. Sci. Lett.*, 411, 199–207, doi:10.1016/j.epsl.2014.10.051, 2015.
- 510 Molli, G., Cortecci, G., Vaselli, L., Ottria, G., Cortopassi, A., Dinelli, E., Mussi, M. and Barbieri, M.: Fault zone structure and fluid-rock interaction of a high angle normal fault in Carrara marble (NW Tuscany, Italy), *J. Struct. Geol.*, 32(9), 1334–1348, doi:10.1016/j.jsg.2009.04.021, 2010.
- Molli, G., White, J. C., Kennedy, L. and Taini, V.: Low-temperature deformation of limestone, Isola Palmaria, northern Apennine, Italy - The role of primary textures, precursory veins and intracrystalline deformation in localization, *J. Struct. Geol.*, 33(3), 255–270, doi:10.1016/j.jsg.2010.11.015, 2011.
- 515 Monzawa, N. and Otsuki, K.: Comminution and fluidization of granular fault materials: Implications for fault slip behavior, *Tectonophysics*, 367(1–2), 127–143, doi:10.1016/S0040-1951(03)00133-1, 2003.
- Niemeijer, A. R. and Spiers, C. J.: Velocity dependence of strength and healing behaviour in simulated phyllosilicate-bearing fault gouge, *Tectonophysics*, 427(1–4), 231–253, doi:10.1016/j.tecto.2006.03.048, 2006.
- 520 Niemeijer, A., Di Toro, G., Nielsen, S. and Di Felice, F.: Frictional melting of gabbro under extreme experimental conditions of normal stress, acceleration, and sliding velocity, *J. Geophys. Res. Solid Earth*, 116(7), 1–18, doi:10.1029/2010JB008181, 2011.
- Oesterling, N., Heilbronner, R., Stünitz, H., Barnhoorn, A. and Molli, G.: Strain dependent variation of microstructure and texture in naturally deformed Carrara marble, *J. Struct. Geol.*, 29(4), 681–696, doi:10.1016/j.jsg.2006.10.007, 2007.
- 525 Ohl, M., Plümpner, O., Chatzaras, V., Wallis, D., Vollmer, C. and Drury, M.: Mechanisms of fault mirror formation and fault healing in carbonate rocks, *Earth Planet. Sci. Lett.*, 530, 115886, doi:10.1016/j.epsl.2019.115886, 2020.
- Paterson, M. S., and Olgaard, D. L.: Rock deformation tests to large shear strains in torsion, *J. Struct. Geol.*, v. 22, p. 1341–1358, 2000.
- Pozzi, G., De Paola, N., Nielsen, S. B., Holdsworth, R. E. and Bowen, L.: A new interpretation for the nature and significance of mirror-like surfaces in experimental carbonate-hosted seismic faults, *Geology*, 46(7), 583–586, doi:10.1130/G40197.1, 2018.
- 530 Pozzi, G., De Paola, N., Holdsworth, R. E., Bowen, L., Nielsen, S. B. and Dempsey, E. D.: Coseismic ultramylonites: An investigation of nanoscale viscous flow and fault weakening during seismic slip, *Earth Planet. Sci. Lett.*, 516, 164–175, doi:10.1016/j.epsl.2019.03.042, 2019.
- Rathbun, A. P. and Marone, C.: Effect of strain localization on frictional behavior of sheared granular materials, *J. Geophys. Res.*, 115(B1), 1–16, doi:10.1029/2009jb006466, 2010.
- 535 Rempe, M., Smith, S., Mitchell, T., Hirose, T. and Di Toro, G.: The effect of water on strain localization in calcite fault gouge sheared at seismic slip rates, *J. Struct. Geol.*, 97, 104–117, doi:10.1016/j.jsg.2017.02.007, 2017.
- Risnes, R., Madland, M. V., Hole, M. and Kwabiah, N. K.: Water weakening of chalk - Mechanical effects of water-glycol mixtures, *J. Pet. Sci. Eng.*, 48(1–2), 21–36, doi:10.1016/j.petrol.2005.04.004, 2005.
- Røyne, A., Bisschop, J. and Dysthe, D. K.: Experimental investigation of surface energy and subcritical crack growth in calcite, *J. Geophys. Res.*, 116(B04204), 10, doi:10.1029/2010jb008033, 2011.
- 540 Rowe, C. D., Moore, J. C., Meneghini, F. and McKeirnan, A. W.: Large-scale pseudotachylytes and fluidized cataclasites from an ancient subduction thrust fault, *Geology*, 33(12), 937–940, doi:10.1130/G21856.1, 2005.
- Rutter, E. H.: The effects of strain-rate changes on the strength and ductility of Solenhofen limestone at low temperature and confining pressure, *Int. J. Rock Mech. Min. Sci.*, 9, 183–189, 1972.



- 545 Rutter, E. H.: Experimental study of the influence of stress, temperature, and strain on the dynamic recrystallization of Carrara marble, *J. Geophys. Res.*, 100(B12), 24651, doi:10.1029/95jb02500, 1995.
- Rutter, E. H., Maddock, R. H., Hall, S. H. and White, S. H.: Comparative microstructures of natural and experimentally produced clay-bearing fault gouges, *Pure Appl. Geophys.*, 124(1–2), 3–30, doi:10.1007/BF00875717, 1986.
- Samtani, M., Dollimore, D. and Alexander, K. S.: Comparison of dolomite decomposition kinetics with related carbonates and the effect of procedural variables on its kinetic parameters, *Thermochim. Acta*, 393, 135–145, 2002.
- 550 Sarnes, B. and Schrüfer, E.: Determination of the time behaviour of thermocouples for sensor speedup and medium supervision, *Proc. Est. Acad. Sci. Eng.*, 13(4), 295–309, 2007.
- Schmid, S. M., Paterson, M. S. and Boland, J. N.: High temperature flow and dynamic recrystallization in Carrara marble, *Tectonophysics*, 65, 245–280, 1980.
- 555 Schmid, S. M., Panozzo, R. and Bauer, S.: Simple shear experiments on calcite rocks: rheology and microfabric, *J. Struct. Geol.*, 9(5–6), 747–778, doi:10.1016/0191-8141(87)90157-X, 1987.
- Sibson, R. H.: Conditions for fault-valve behaviour, in *Deformation Mechanisms, Rheology and Tectonics*, vol. 54, edited by R. J. Knipe and E. H. Rutter, pp. 15–28, Geological Society Special Publication., 1990.
- Smeraglia, L., Billi, A., Carminati, E., Cavallo, A. and Doglioni, C.: Field- to nano-scale evidence for weakening mechanisms along the fault of the 2016 Amatrice and Norcia earthquakes, Italy, *Tectonophysics*, 712–713, 156–169, doi:10.1016/j.tecto.2017.05.014, 2017.
- 560 Snoke, A. W., Tullis, J., Todd, V. R.: *Fault-Related Rocks: a Photographic Atlas*, Princeton Univ. Press, Princeton, N.J., 1998.
- Smith, S. A. F., Di Toro, G., Kim, S., Ree, J.-H., Nielsen, S. B., Billi, A. and Spiess, R.: Coseismic recrystallization during shallow earthquake slip, *Geology*, 41(1), 63–66, doi:10.1130/G33588.1, 2013.
- Smith, S. A. F., Nielsen, S. and Di Toro, G.: Strain localization and the onset of dynamic weakening in calcite fault gouge, *Earth Planet. Sci. Lett.*, 413, 25–36, doi:10.1016/j.epsl.2014.12.043, 2015.
- 565 Smith, S. A. F., Griffiths, J. R., Fondriest, M. and Di Toro, G.: ‘Coseismic Foliations’ in Gouge and Cataclasite: Experimental Observations and Consequences for Interpreting the Fault Rock Record, in *Fault Zone Dynamic Processes: Evolution of Fault Properties During Seismic Rupture*, edited by M. Y. Thomas, T. M. Mitchell, and H. S. Bhat, pp. 81–102, Geophysical Monograph., 2017.
- Tesei, T., Collettini, C., Barchi, M. R., Carpenter, B. M. and Di Stefano, G.: Heterogeneous strength and fault zone complexity of carbonate-bearing thrusts with possible implications for seismicity, *Earth Planet. Sci. Lett.*, 408, 307–318, doi:10.1016/j.epsl.2014.10.021, 2014.
- 570 Tesei, T., Carpenter, B. M., Giorgetti, C., Scuderi, M. M., Sagy, A., Scarlato, P. and Collettini, C.: Friction and scale-dependent deformation processes of large experimental carbonate faults, *J. Struct. Geol.*, 100, 12–23, doi:10.1016/j.jsg.2017.05.008, 2017.
- Trouw, R. A., Passchier, C. W., Wiersma, D. J.: *Atlas of Mylonites-and related microstructures*, Springer Science & Business Media, 2009.
- Ungár, T.: Microstructural parameters from X-ray diffraction peak broadening, *Scr. Mater.*, 51(8 SPEC. ISS.), 777–781, doi:10.1016/j.scriptamat.2004.05.007, 2004.
- 575 Verberne, B. A., Spiers, C. J., Niemeijer, A. R., de Bresser, J. H. P., de Winter, D. A. M. and Plümpner, O.: Frictional properties and microstructure of calcite-rock fault gouges sheared at sub-seismic velocities., *Pure Appl. Geophys.*, 31(0), 1–45, doi:10.1007/s00024-013-0760-0, 2014.
- Viola, G., Mancktelow, N. S. and Miller, J. A.: Cyclic frictional-viscous slip oscillations along the base of an advancing nappe complex: Insights into brittle-ductile nappe emplacement mechanisms from the Naukluft Nappe Complex, central Namibia, *Tectonics*, 25(3), 1–20, doi:10.1029/2005TC001939, 2006.
- 580



- Violay, M. E. S., Nielsen, S. B., Gibert, B., Spagnuolo, E., Cavallo, A., Azais, P., Vinciguerra, S. C. and Di Toro, G.: Effect of water on the frictional behavior of cohesive rocks during earthquakes, *Geology*, 42(1), 27–30, doi:10.1130/G34916.1, 2014.
- Wallis, D., Phillips, R. J. and Lloyd, G. E.: Fault weakening across the frictional-viscous transition zone, Karakoram Fault Zone, NW Himalaya, *Tectonics*, 32(5), 1227–1246, doi:10.1002/tect.20076, 2013.
- 585 Weeks, J. D. and Tullis, T. E.: Frictional sliding of dolomite: A variation in constitutive behavior, *J. Geophys. Res.*, 90(B9), 7821–7826, doi:10.1029/JB090iB09p07821, 1985.
- Williams, J.C.: The segregation of particulate materials. A review, *Powder Technology* 15, 245-251, [https://doi.org/10.1016/0032-5910\(76\)80053-8](https://doi.org/10.1016/0032-5910(76)80053-8), 1976.

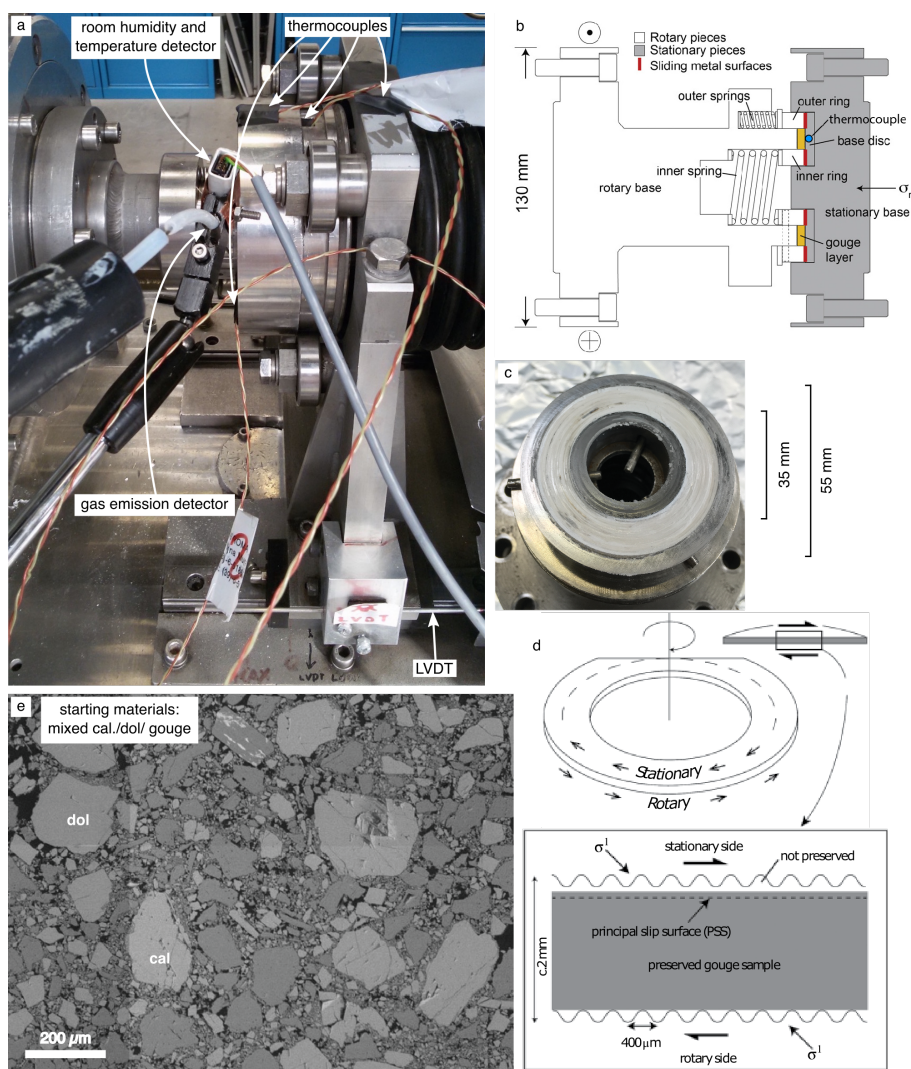


Figure 1. Rotary-shear experimental setup. a) Detectors in the sample chamber. Gas emission, humidity, and temperature detectors were placed at <1 cm from the sample holder. Four thermocouples were placed on the stationary side at increasing distances from the gouge layer. Note: the position of the thermocouple nearest to the gouge layer is not visible here and is illustrated in b). b) Diagram of the gouge holder with the location of the thermocouple nearest to the gouge layer (modified after Smith et al., 2015). c) Sample appearance post deformation with mirror-like slip surface formed in an experiment performed at $V = 0.1 \text{ ms}^{-1}$. d) Diagram showing the location of the recovered and analysed gouge layer after the experiment (after Smith et al., 2017). e) SEM backscattered electron (SEM-BSE) image of the starting material after applying 17.5 MPa for 300 s.

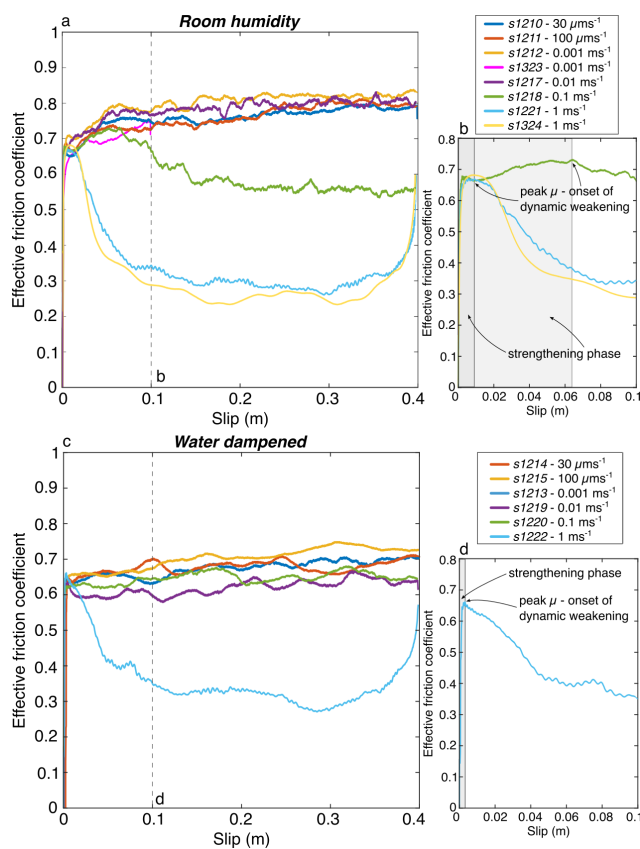


Figure 2. Effective friction coefficient in mixed calcite-dolomite gouges. a) and c) Effective friction coefficient versus slip under room humidity and water dampened conditions. c) and d) Detail of effective friction coefficient versus slip in the first 0.1 m of slip in experiments where slip-weakening was observed.

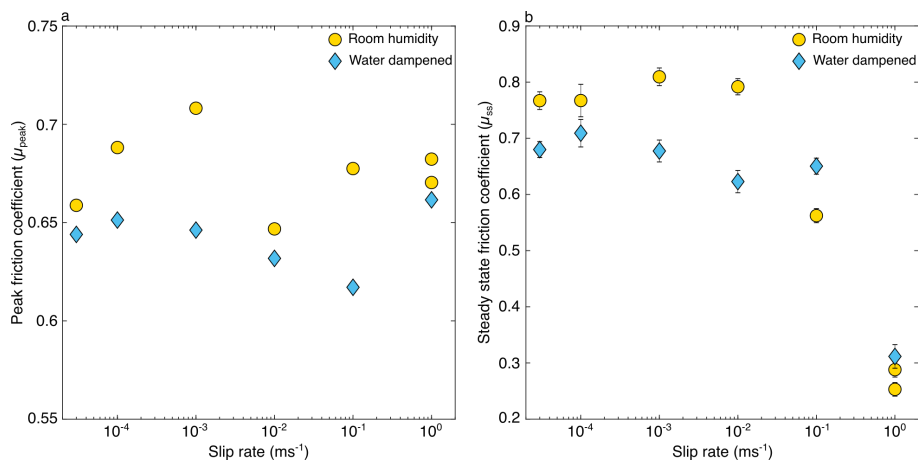


Figure 3. Peak and steady state friction coefficient. a) For experiments that showed slip strengthening, the peak friction coefficient was calculated just before the onset of strengthening behaviour in the first 0.1 m of slip. For experiments showing dynamic weakening, the peak friction immediately precedes the friction drop (see Fig. 2b and 2d). b) Steady state friction coefficient was calculated at displacements between 0.15 m and 0.35 m.

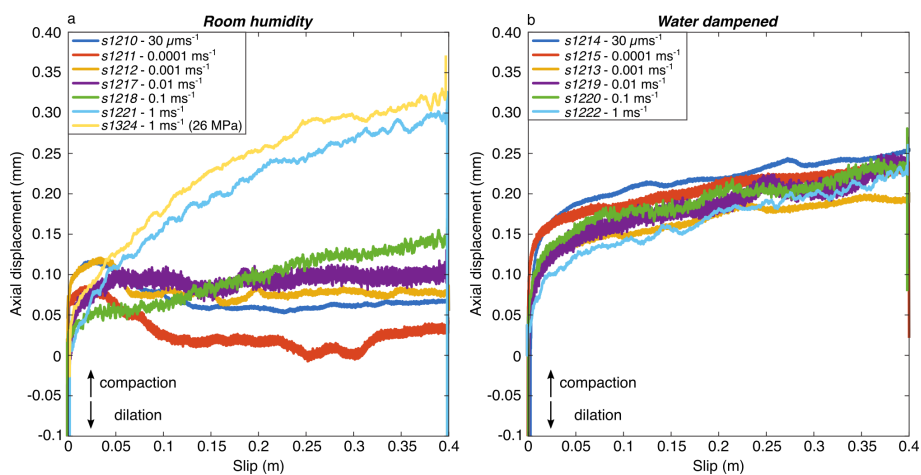


Figure 4. Gouge thickness evolution with slip and slip rate. a) Under room humidity conditions and for slip rates of $V \leq 0.01 \text{ ms}^{-1}$, an initial dilation phase (lasting 0.1-0.15 m) was followed by a period of no compaction or dilation was observed. Instead, at higher slip rates ($V \geq 0.1 \text{ ms}^{-1}$), the gouge compacted constantly throughout the whole experiment, with compaction rate increasing with slip rate. b) Under water dampened conditions, the gouge compacted at a similar rate at all investigated slip rates.

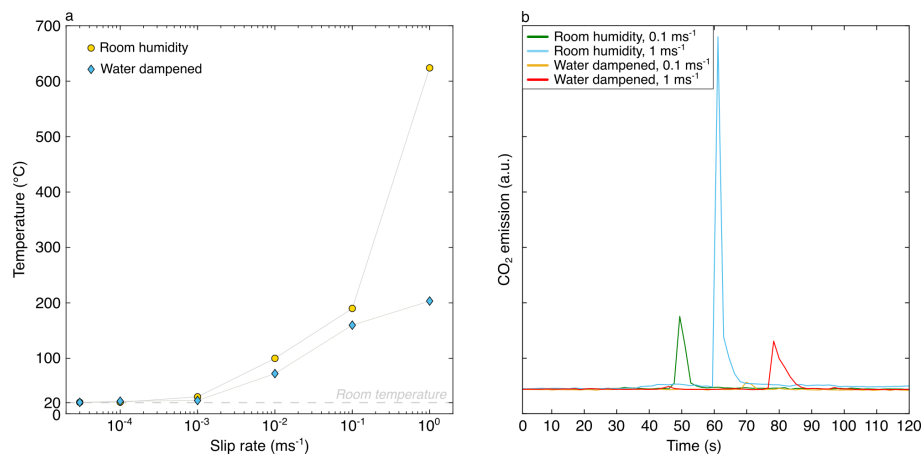


Figure 5. Peak temperatures and CO₂ emissions. a) Maximum temperature measured by the thermocouple located closest to the gouge layer (see Fig. 1b for location). b) CO₂ emissions for experiments at $V \geq 0.1 \text{ ms}^{-1}$ in both room humidity and water dampened conditions. Greater emissions occur at room humidity conditions, but smaller and distinct peaks are also observed in the presence of water.

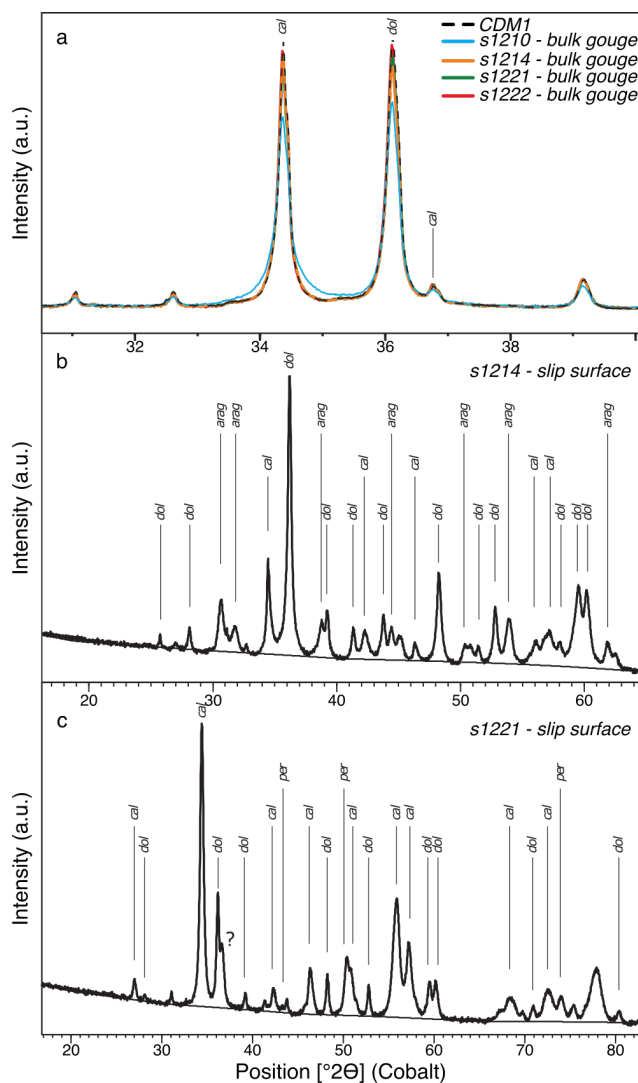


Figure 6. XRPD analysis of bulk gouge and slip surfaces. a) Bulk gouge shows a Lorentzian profile for the main calcite peak in experiment *s1210*, suggesting either a large crystallite size distribution or microstrain as a result of intense comminution involving a large fraction of the gouge. b) At $30 \mu\text{ms}^{-1}$ in water dampened conditions, traces of aragonite are found on the slip surface as a result of calcite polymorphic transformation during prolonged mechanical grinding. c) For *s1221* (1ms^{-1} in room humidity conditions), presence of Mg-calcite and periclase (MgO) on the mirror-like slip surface is observed due to decarbonation of dolomite.

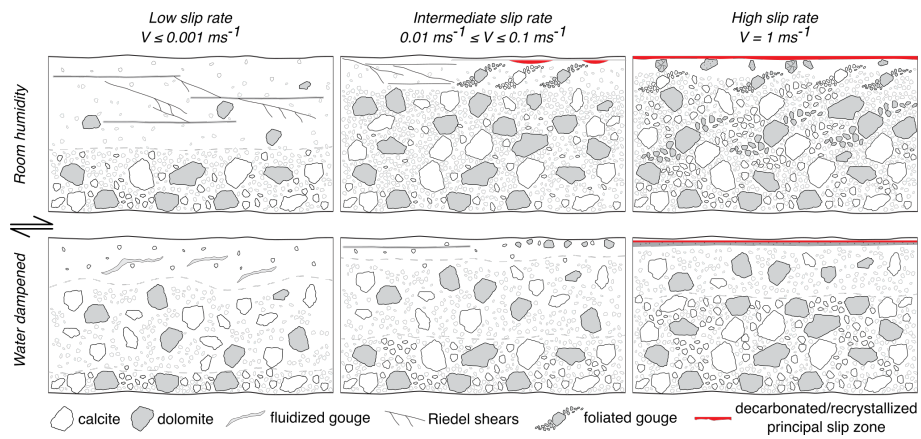


Figure 7. Summary of microstructural evolution at different slip rates and deformation conditions.

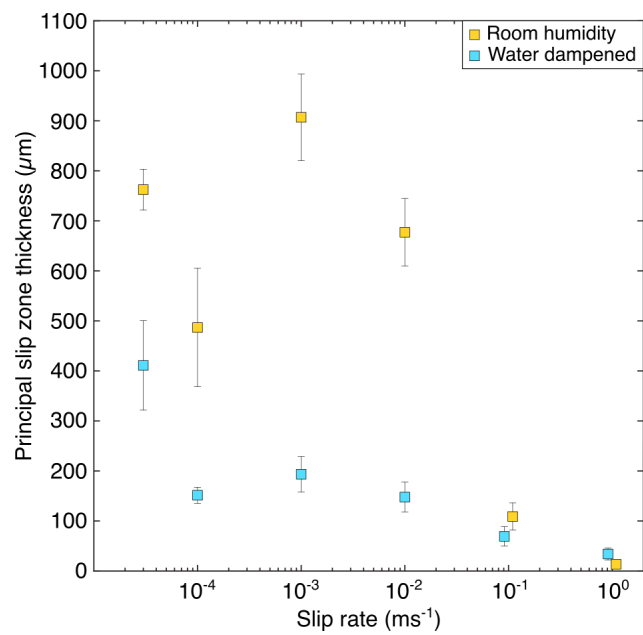


Figure 8. Slip zone thickness evolution with slip rate and ambient conditions. The thickness of the localized slip zone decreases almost linearly with $\log(V)$ in water dampened experiments. For room humidity conditions, partial sample loss after the experiment means slip zone thickness values are a minimum estimate.

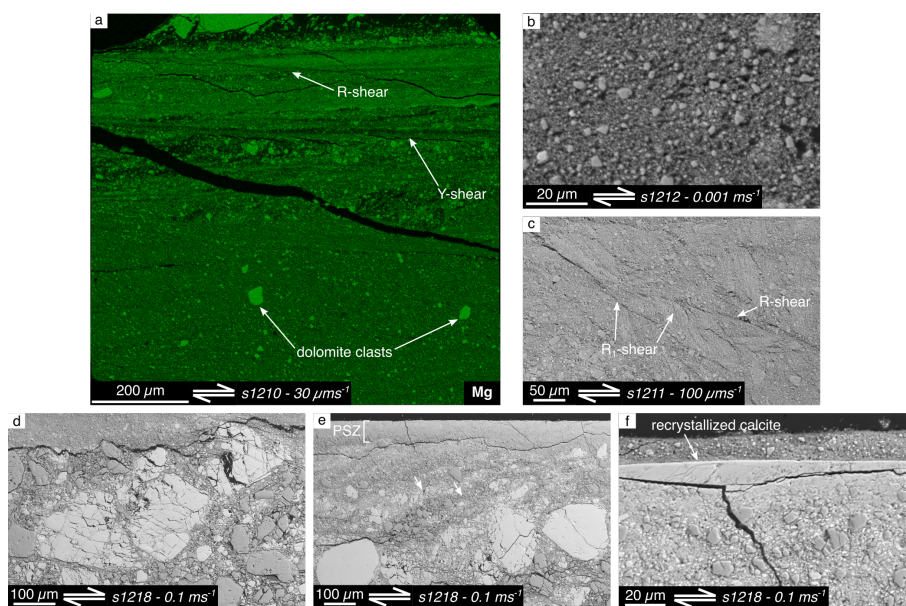


Figure 9. Microstructures of experiments in room humidity conditions and $V \leq 0.1 \text{ ms}^{-1}$. a) Mg element map of the thick slip zone highlighting the location of remnant dolomite clasts. b) Detail of the fine-grained matrix in the slip zone made of a calcite-dolomite mixture with surviving sub-rounded dolomite clasts up to few tens of micrometres in size. c) The fine-grained slip zone is commonly cut by Y-, R- and R_1 -shear bands crosscutting each other. d) Enhanced grain size reduction in calcite grains due to fracturing along cleavage planes. e) Development of a weak foliation adjacent to the principal slip zone at $V = 0.1 \text{ ms}^{-1}$. f) Patches of dynamically recrystallized calcite along the principal slip zone at $V = 0.1 \text{ ms}^{-1}$.

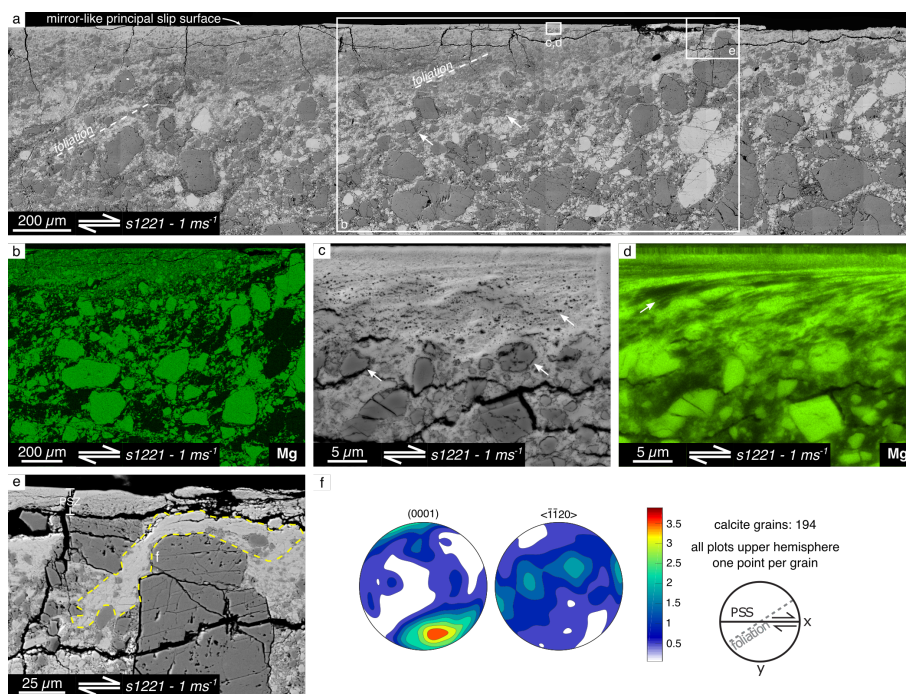


Figure 10. Microstructures of experiments in room humidity conditions and $V = 1 \text{ ms}^{-1}$. a) Development of a foliation consisting in alternation of calcite- and dolomite-rich domains, antithetically inclined $c. 40^\circ$ from the PSS and becoming subparallel to the gouge boundaries when approaching the PSS. Larger dolomite (and when present calcite) clasts have tails of fine-grained material, resembling mantled porphyroclasts. b) Mg element map highlighting foliation development in the bulk gouge. c) Dolomite clasts adjacent to the principal slip zone are characterized by internal holes and vesicular rims interpreted as due to degassing during dolomite decarbonation reaction. Banding of low and higher porosity in the principal slip zone is an indicator for dolomite content. d) Mg element map of c) showing dolomite and calcite banding in the principal slip zone. e) Transition from the principal slip zone to the underlying fractured and foliated gouge with calcite showing evidence of dynamic recrystallization. f) Orientation data for calcite in area highlighted in e). showing the development of a clear CPO along the c-axes.

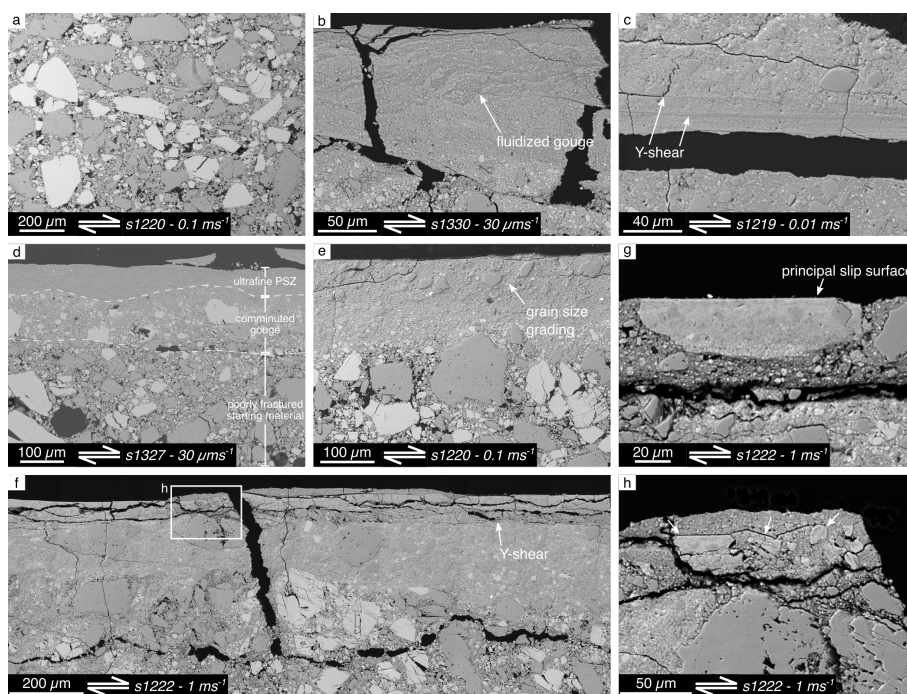


Figure 11. Microstructures of experiments in water dampened conditions. a) The bulk gouge is made of poorly fractured calcite and dolomite mixture highly resembling the starting material. b) Occurrence of fluidized structures in the principal slip zone of experiments performed at $30 \mu\text{ms}^{-1}$. c) At $0.0001 \text{ ms}^{-1} \leq V < 0.1 \text{ ms}^{-1}$, the principal slip zone is cut by multiple Y-shears. d) In the presence of fluid water, an ultrafine principal slip surface develops, overlying a highly comminuted gouge which then transitions to a poorly fractured starting material. e) At $V = 0.1 \text{ ms}^{-1}$, grain size grading is observed in the principal slip zone, with larger clasts occurring near the principal slip surface. f) At $V = 1 \text{ ms}^{-1}$, strain localizes on a compacted, low porosity, recrystallized slip zone, which g) is not continuous and h) often found broken and reworked.



Table 1. Experiments reported in this study.

Experiment	Experimental conditions	Target slip rate ms ⁻¹	Displacement m	Normal stress MPa	Mixture batch
s1322	Room humidity	0.00003	0.1	17.4	CDM2
s1210	Room humidity	0.00003	0.4	17.4	CDM1
s1211	Room humidity	0.0001	0.4	17.4	CDM1
s1323	Room humidity	0.001	0.1	17.4	CDM2
s1212	Room humidity	0.001	0.4	17.4	CDM1
s1217	Room humidity	0.01	0.4	17.4	CDM1
s1218	Room humidity	0.1	0.4	17.4	CDM1
s1221	Room humidity	1	0.4	17.4	CDM1
s1324	Room humidity	1	0.4	17.4	CDM2
s1327	Water dampened	0.00003	0.05	17.4	CDM2
s1329	Water dampened	0.00003	0.1	17.4	CDM2
s1328	Water dampened	0.00003	0.2	17.4	CDM2
s1214	Water dampened	0.00003	0.4	17.4	CDM1
s1330	Water dampened	0.00003	0.4	17.4	CDM2
s1215	Water dampened	0.0001	0.4	17.4	CDM1
s1213	Water dampened	0.001	0.4	17.4	CDM1
s1219	Water dampened	0.01	0.4	17.4	CDM1
s1220	Water dampened	0.1	0.4	17.4	CDM1
s1222	Water dampened	1	0.4	17.4	CDM1
<i>Static load</i>	sld	Room humidity		17.4	CDM1
	slw	Water dampened		17.4	CDM2